

Supporting Information

Reveal and Control of Chiral Cathodoluminescence at Subnanoscale

Tianyang Han^{1‡}, Shuai Zu^{1‡}, Ziwei Li¹, Meiling Jiang¹, Xing Zhu¹, and Zheyu Fang^{1,}*

¹School of Physics, State Key Lab for Mesoscopic Physics, Peking University, Beijing 100871,
China.

*E-mail: zhyfang@pku.edu.cn

Contents

I. CL measurements

II. Selection of wavelength range for the circularly polarized CL detection

III. Selection of electron-beam impinging positions on the heptamer nanostructure

IV. Multipole expansion calculation of the CL response in the heptamer nanostructure

V. Calculation of the CL helicity switch distance

VI. CL chirality of a compact heptamer nanostructure

VII. CL helicity of the mirrored heptamer nanostructure

VIII. CL chirality evolution with the heptamer changing from chiral to achiral

I. CL measurements

CL images and spectra were acquired by a CL spectrograph/detector system (Gatan MonoCL4 Plus), which is equipped onto the SEM (FEI Quanta 450 FEG). Figure S1a shows the optical path for panchromatic CL collection, which means that the emission is collected by the photomultiplier tube (PMT, 160-930 nm) without passing through the spectrometer. For detecting specific wavelength of the emission, filters can be placed in the optical path. For example, the 695 nm long pass filter (Thorlabs, FGL695) is used for acquiring the CL image (Figure 2a) in the main text. For circularly polarized CL detection, a quarter-wave plate (QWP, Thorlabs, AQWP10M-980) and a linear polarizer (Thorlabs, LPVIS100) are used. The LCP and RCP emissions can be selectively collected by rotating the QWP by $\pm 45^\circ$ with respect to the polarization axis of the polarizer. Figure S1b displays the optical path for monochromatic CL collection, which means that the emission passes through the spectrometer before collected. The CL emission is dispersed by a 1200 lines/mm grating, and the CL spectrum can be acquired by recording the PMT counts of each wavelength by rotating the grating (2.5 nm/step). Besides, the substrate background signal is subtracted from raw spectra, and the resulting spectra are corrected based on the collection efficiency of the system.

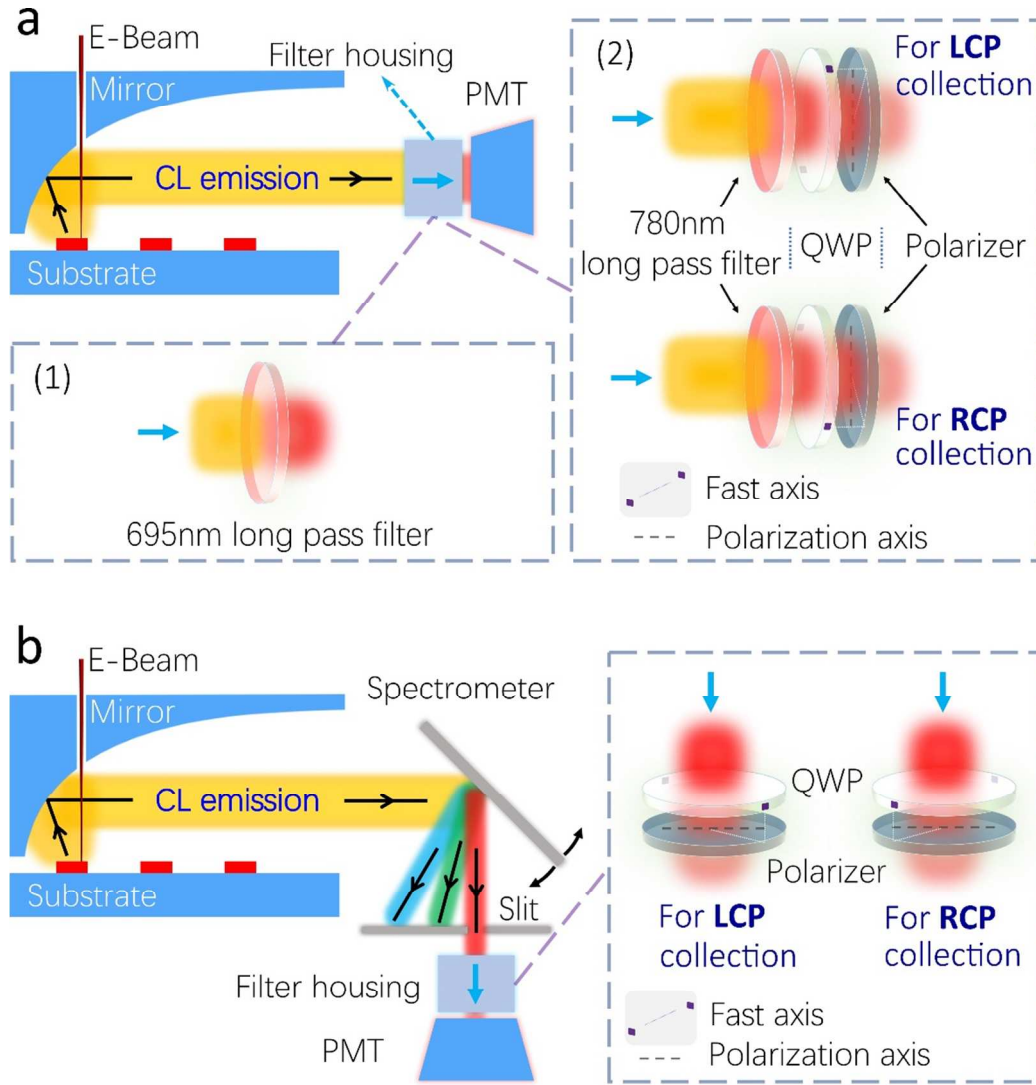


Figure S1. Schematic of the experimental measurement setup. (a) Optical path for the panchromatic CL collection. (1) 695 nm long pass filter applied in Figure 2a. (2) Filter groups applied to collect the RCP and LCP CL images respectively for Figure 4a. (b) Optical path for the monochromatic CL collection, which is used to obtain spectra in Figure 2c-e. Blue arrows in all of the schematics indicate the propagation direction of light.

II. Selection of wavelength range for the circularly polarized CL detection

The CL helicity change originates from the plasmon modes switching when changing the electron impinging position (Figure 3). Specifically, when the electron-beam impinges on the

ends of the ellipse, the coupling between adjacent ellipses leads to an alignment of dipoles along the ellipse major axis, which contributes to the RCP CL emission. Therefore, we chose the wavelength range of the ellipse major axis dipole mode for the following CL detection and analysis to minimize the influence of the dipole mode along the minor axis.

In Figure S2, the CL images at wavelengths from 550 nm to 850 nm are displayed. It exhibits a transition process from dipole mode along the minor axis to the one along the major axis when the detection wavelength increases. At 650 nm, dipole modes along the minor and major axes present almost the same intensity (Figure S2c). However, at 700 nm, dipole mode along the major axis is dominated (Figure S2d). We hence used a 695 nm long pass filter to determine the electron-beam impinging positions (Figure 2a), and measured all of the circularly polarized CL spectra from 690 nm (Figure 2c-e). Besides, the reduction of the PMT quantum efficiency makes the collected signal intensity comparable to the background noise level after 890 nm, thus the CL spectrum cannot be effectively captured. As a result, the wavelength range from 690 nm to 890 nm was chosen to perform the following measurements.

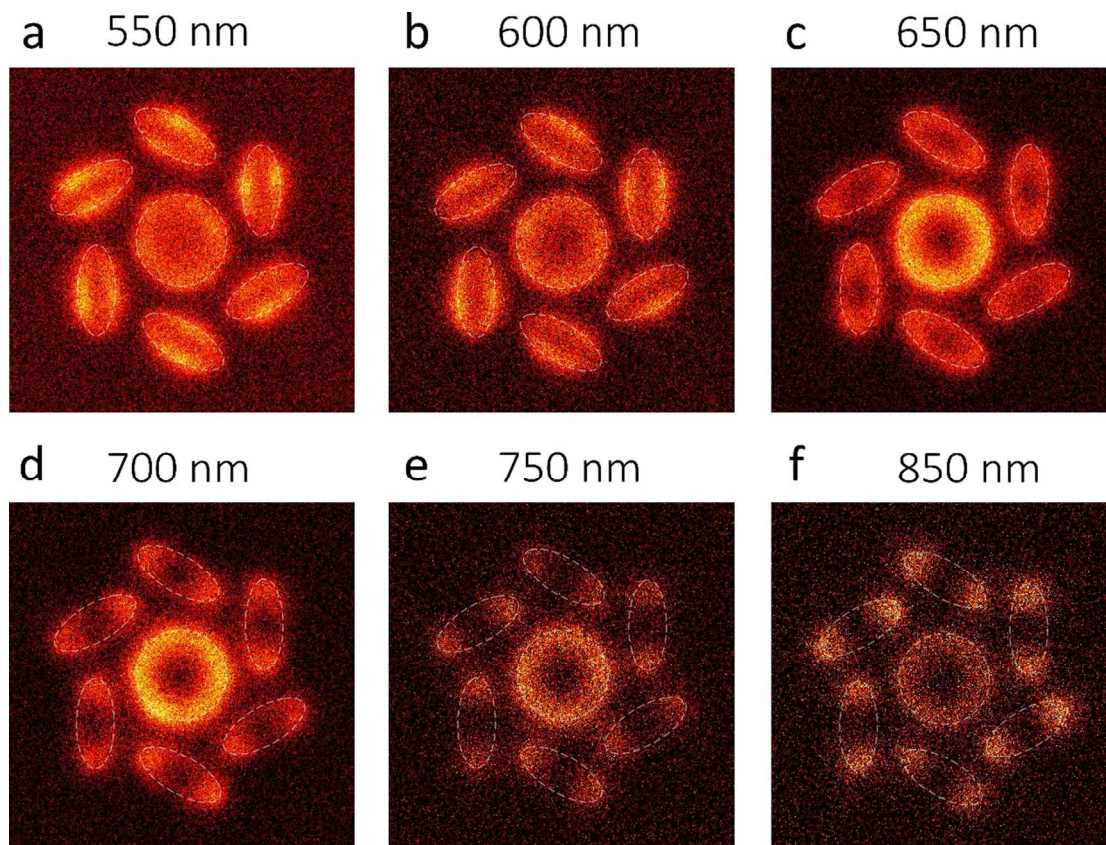


Figure S2. CL images of the heptamer with different band pass filters. Images were acquired utilizing the optical path in Figure S1a with band pass filters from 550nm to 850nm, which displays the variation of dipole oscillation on the ellipses that changed from the minor axis to the major axis with the increase of the detection wavelength.

III. Selection of electron-beam impinging positions on the heptamer nanostructure

The C_{6h} centrosymmetry of the heptamer guarantees the same spectral properties of each ellipse. However, the radiation direction for each ellipse is different. To ensure the minimal CL distortion induced by the parabolic mirror, the electron-beam impinging positions marked in Figure 2a are chosen, because for these impinging positions, most of the radiation from the heptamer is emitted towards the regions of the parabolic mirror with largest curvature, preserving the helicity of the radiation.¹

IV. Multipole expansion calculation of the CL response in the heptamer nanostructure

To provide better insight into the origin of the chiral CL emission, multipole expansion method was used to analyze the plasmonic modes and the multipole contributions from different multipole moments. For a current source distribution in the nanostructure, the total scattering power can be expanded as the sum of the multipole radiation. In the case of harmonic excitation $\exp(i\omega t)$, it has the form^{2,3}

$$\begin{aligned}
 I &= \frac{1}{12\pi\epsilon_0\epsilon_r c^3} \left[\left(\ddot{\mathbf{p}} - \frac{1}{c^2} \ddot{\mathbf{T}} \right)^2 + \frac{|\ddot{\mathbf{m}}|^2}{c^2} \right] + \frac{1}{160\pi\epsilon_0\epsilon_r c^5} \sum |\ddot{Q}_{\alpha\beta}|^2 + \frac{1}{160\pi\epsilon_0\epsilon_r c^7} \sum |\ddot{M}_{\alpha\beta}|^2 \\
 &= \frac{\omega^4}{12\pi\epsilon_0\epsilon_r c^3} |\mathbf{p}|^2 + \frac{\omega^4}{12\pi\epsilon_0\epsilon_r c^5} |\mathbf{m}|^2 + \frac{\omega^6}{12\pi\epsilon_0\epsilon_r c^7} |\mathbf{T}|^2 - \frac{i\omega^5}{12\pi\epsilon_0\epsilon_r c^5} (\mathbf{p}^* \cdot \mathbf{T} - \mathbf{p} \cdot \mathbf{T}^*) \\
 &\quad + \frac{\omega^6}{160\pi\epsilon_0\epsilon_r c^5} \sum |Q_{\alpha\beta}|^2 + \frac{\omega^6}{160\pi\epsilon_0\epsilon_r c^7} \sum |M_{\alpha\beta}|^2
 \end{aligned}$$

(S1)

The first two terms correspond to the electric and magnetic dipole scattering. The third term corresponds to the toroidal dipole scattering and the fourth term accounts for the coupling between the electric and toroidal dipoles. The fifth and sixth terms come from electric and magnetic quadrupoles. The multipole moments in the above equation are defined as:

$$\text{electric dipole moment: } \mathbf{p} = \frac{1}{i\omega} \int \mathbf{j} d^3r$$

$$\text{magnetic dipole moment: } \mathbf{m} = \frac{1}{2} \int (\mathbf{r} \times \mathbf{j}) d^3r$$

$$\text{electric quadrupole moment: } Q_{\alpha\beta} = \frac{1}{i\omega} \int \left[r_\alpha j_\beta + r_\beta j_\alpha - \frac{2}{3} (\mathbf{r} \cdot \mathbf{j}) \delta_{\alpha\beta} \right] d^3r$$

$$\text{magnetic quadrupole moment: } M_{\alpha\beta} = \frac{1}{3} \int \left[(\mathbf{r} \times \mathbf{j})_\alpha r_\beta + (\mathbf{r} \times \mathbf{j})_\beta r_\alpha \right] d^3r$$

$$\text{toroidal dipole moment: } \mathbf{T} = \frac{1}{10} \int \left[(\mathbf{r} \cdot \mathbf{j}) \mathbf{r} - 2r^2 \mathbf{j} \right] d^3r$$

where c is the speed of light in medium, \mathbf{j} is the current density, and $\alpha, \beta = x, y, z$.

Figure S3 shows the radiation powers from each term as a function of wavelength for the three impinging positions in Figure 3. With the electron-beam excitation, the higher-order resonance modes are excited for all the three positions, which is the prerequisite for the chiral CL emission. However, the multipole contributions for the disk excitation and the ellipse excitation are different, giving rise to the difference in the chirality of CL emissions. In detail, the scattering power mainly comes from the electric dipole, the magnetic quadrupole, toroidal dipole and the coupling between the electric and toroidal dipoles for the disk excitation, while the ellipse excitations also induce strong magnetic dipole and electric quadrupole responses. The major difference between the disk excitation and the ellipse excitation is in the contributions from the magnetic dipole and the electric quadrupole modes, leading to the change of chirality in CL emissions. From this decomposition, we can clearly see the origin of chirality in the CL spectra and the change of chirality for different excitation positions.

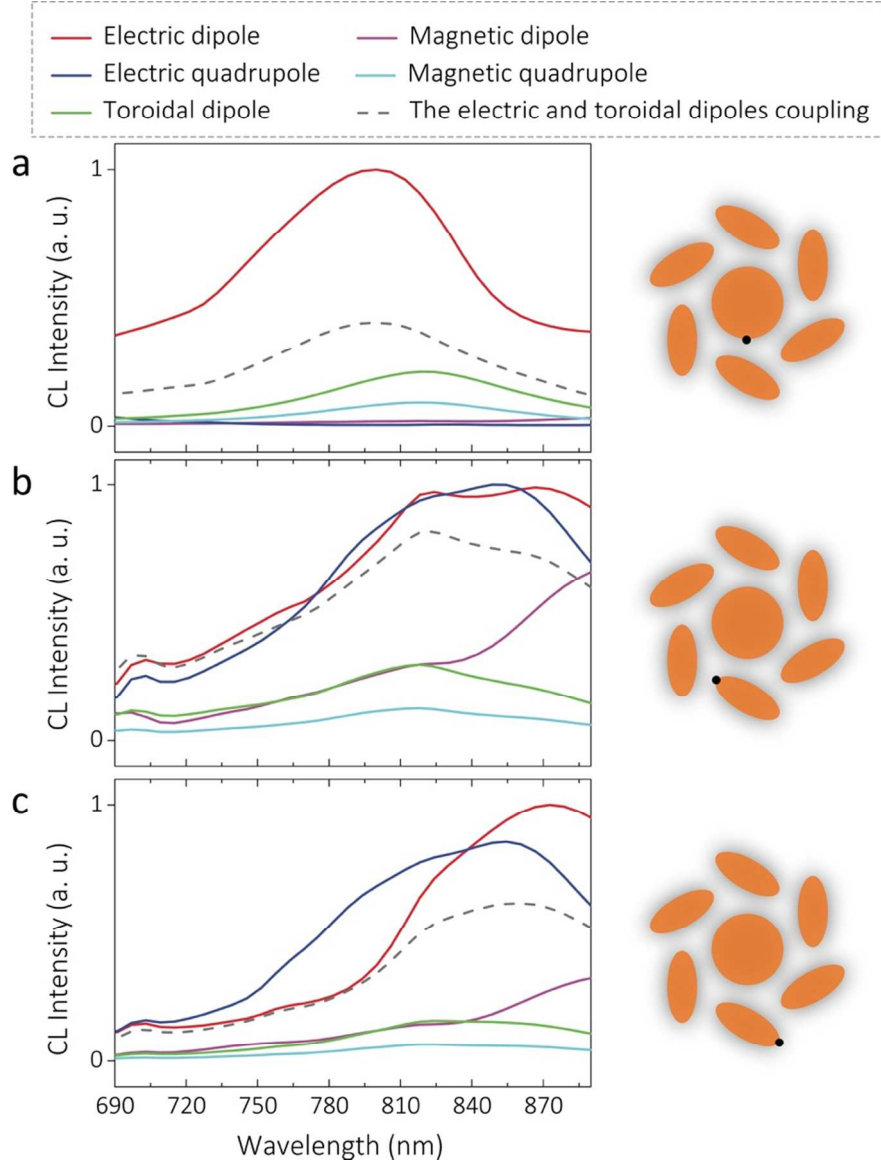


Figure S3. Multipole contributions to the CL spectra corresponding to the three impinging positions as shown in Figure 3. The magnetic dipole and the electric quadrupole responses show significant differences between the disk excitation (a) and the ellipse excitation (b, c).

V. Calculation of the CL helicity switch distance

Circularly polarized CL images (Figure S4a,b) were acquired by the optical path shown in Figure S1a. A 780 nm long pass filter was used to collect the circularly polarized CL signals after 780 nm for increasing the signal to noise ratio (SNR). At this wavelength range, the heptamer exhibits large Δ CL response and the CL helicity switch can be clearly presented. The circularly polarized CL images are aligned based on the synchronized SEM images. Both images are composed of 495*495 pixels with the side length of 739 nm. The Δ CL image (Figure S4c) is plotted by making a subtraction between Figure S4a,b.

Each pixel can be represented by utilizing the coordinates shown in Figure S4c. Based on the relationship between the number of pixels and the side length, we can deduce the electron-beam scan step (pixel to pixel distance) ΔL is 1.49 nm both along x and y axes.

Paths referred in Figure 4b-d can be defined by the coordinates from (M_1, N_1) to (M_2, N_2) with the length of $|M_2 - M_1|$ pixels and $|N_2 - N_1|$ pixels along x and y axes, respectively. The number of data points on Path α is chosen as the maximum one of $|M_2 - M_1| + 1$ and $|N_2 - N_1| + 1$, which also corresponds to the maximum that prevents adjacent data points locating in the same pixel. Hence, the distance between adjacent points is

$$\sqrt{(M_2 - M_1)^2 + (N_2 - N_1)^2} \times \Delta L / \text{Max}(|M_2 - M_1|, |N_2 - N_1|) \quad (\text{S2})$$

Path α can be defined by the coordinates from (205, 370) to (307, 234), which are marked in Figure S4c. As a result, values of the data points in Figure 4b can be extracted along with Path α by a step of 1.25 pixels (1.86nm). Figure S4d displays a magnified image of the square in Figure S4c. The magnified image of the dashed square in Figure S4d is shown in Figure S4e, in which positions of data points (green points) are displayed.

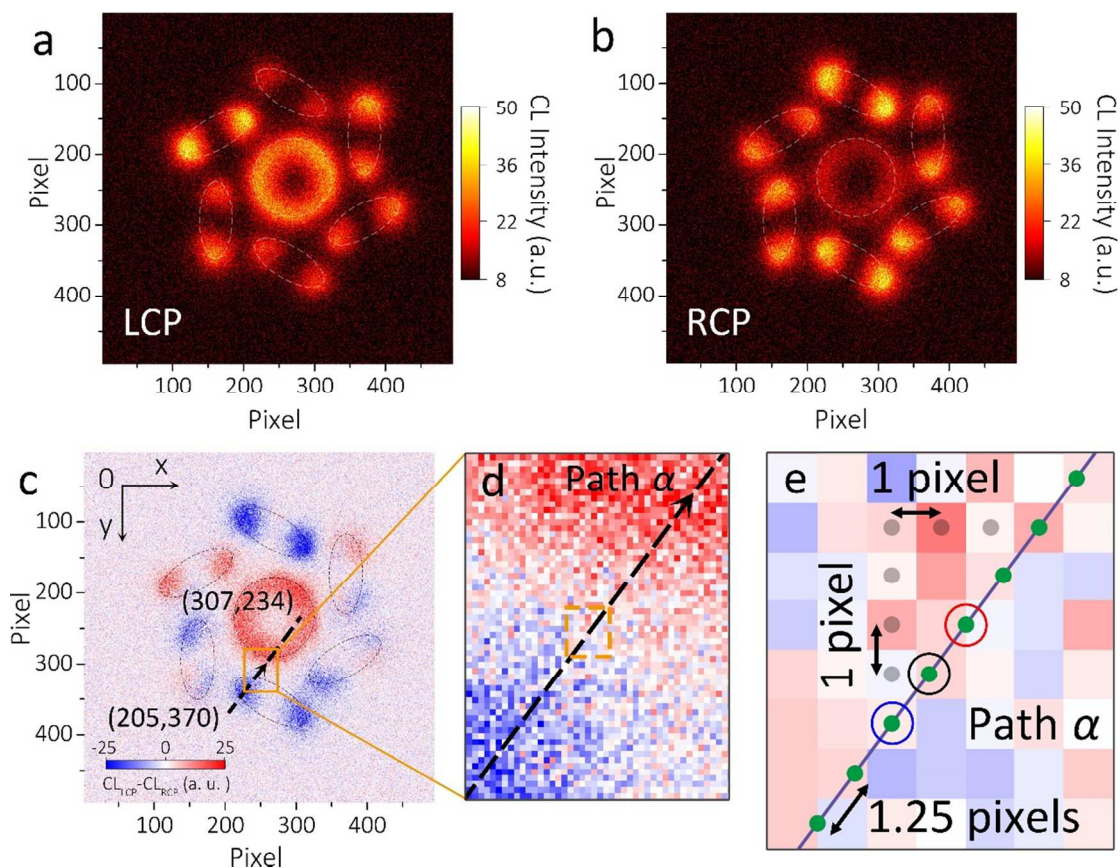


Figure S4. (a, b) LCP and RCP CL images of the heptamer. (c) Δ CL image of the heptamer. (d) Magnified Δ CL image of the region marked by the square in (c). (e) Calculation method of the step distance along Path α .

To better determine the switch distance of helicity, a statistical averaging method was used to calculate the Δ CL value of each point (green ones in Figure S4e) on Path α , which can reduce the uncertainty resulted from only choosing the value of a single pixel. For each green point on Path α , the final Δ CL value is associated with the adjacent yellow points on the line across this point and perpendicular to Path α , as shown in Figure S5. The distance between each yellow point is chosen as 1.25 pixel (1.86 nm) to avoid the case that adjacent yellow points locate in the same pixel.

There are only four possible locations of the green points inside a pixel square (See the inset of Figure S5). For each condition, the 9 corresponding yellow points and their related pixels (dark squares) are settled, and these pixel values can be averaged for the final ΔCL of the green point, as shown in Figure S5a-d. In this way, the ΔCL values of all the data points on Path α were acquired and plotted by the scatter diagram in Figure 4b.

In Figure S3e, the calculated ΔCL of the data point marked by the black circle is 0.11, which is also marked in Figure 4b (Green circle in the Main Text). It can be considered as the achiral region compared with the adjacent data points (marked by the blue and red circles with the ΔCL value of -3.11 and 2, respectively). As a result, a CL helicity switch from LCP (RCP) to achiral emission can happen within 1.86 nm (1.25 pixels) of the electron-beam movement. The same calculation method was also applied to Path β and γ , and the results are shown in Figure 4c,d, respectively.

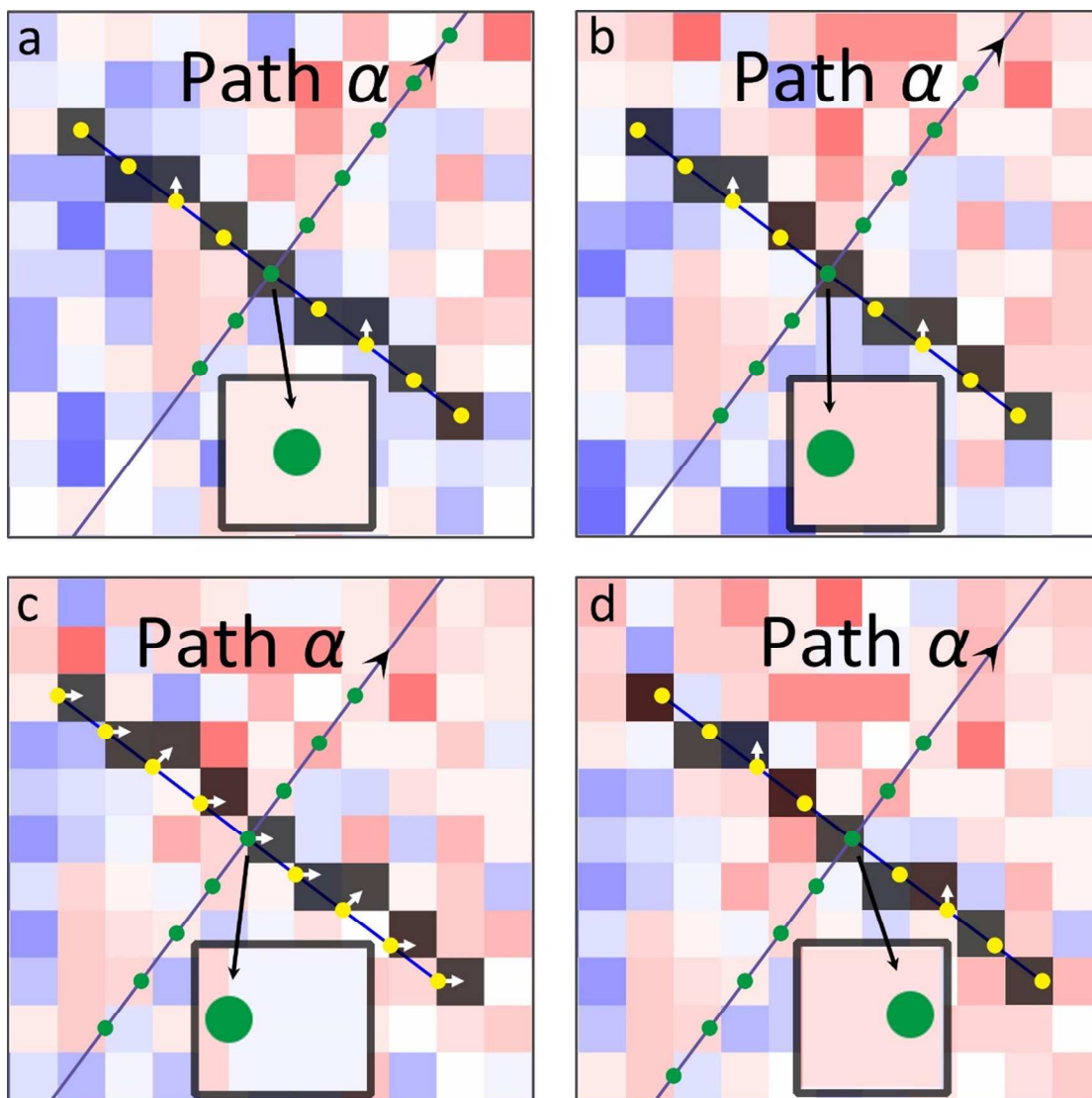


Figure S5. Selecting method of pixels for the averaged ΔCL calculation. (a-d) Four kinds of pixel selecting methods based on the green point location inside the pixel square are displayed. The green points are part of the data points on Path α . The dark squares in each panel present the chosen pixels for taking the averaged ΔCL . White arrows specify the yellow points and their corresponding pixels (dark squares).

VI. CL chirality of a compact heptamer nanostructure

We simulated the circularly polarized CL spectra with a center to center distance of 160 nm between the disk and the surrounding ellipses (Figure S6a-c) in comparison with the 180 nm

distance in our experiment for the main text. Compared with the FDTD simulated results in Figure 3, the compact heptamer presents similar results for the three electron-beam impinging positions.

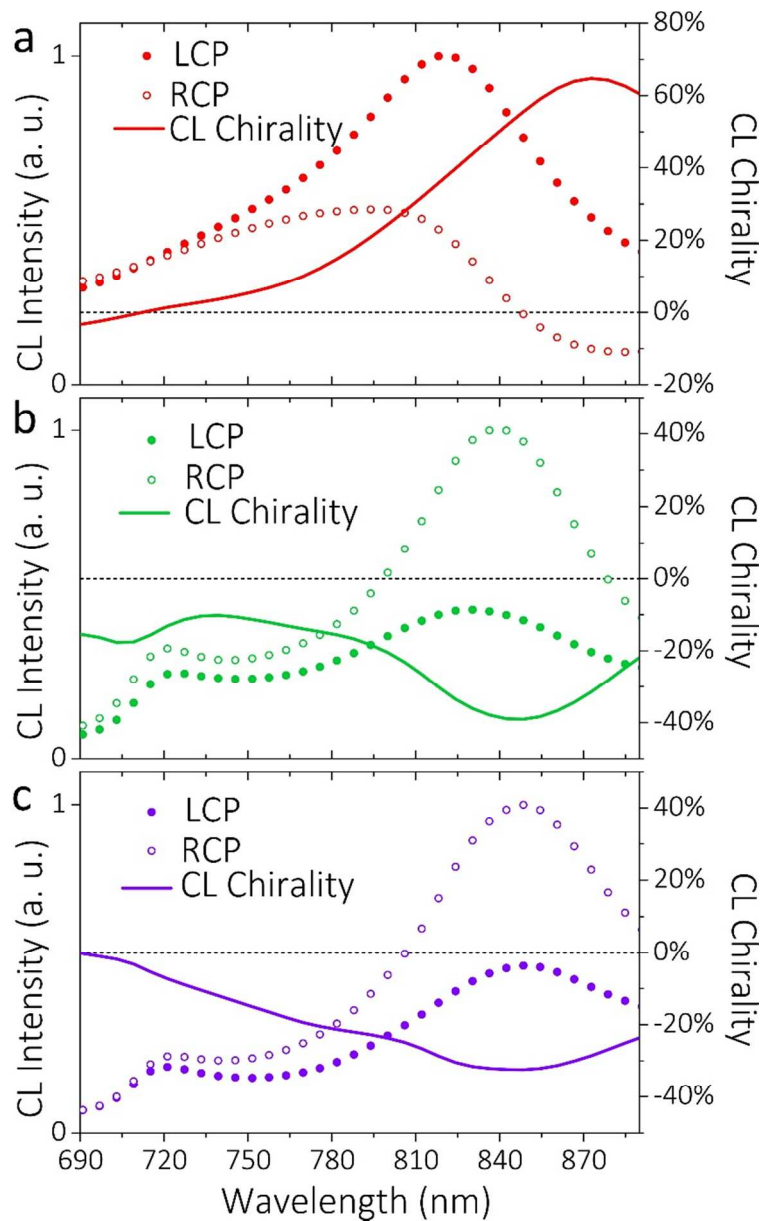


Figure S6. Simulated circularly polarized CL emissions of the heptamer with 160 nm center-center distance between the disk and ellipses for the three electron-beam impinging positions as marked in Figure 3d-f.

VII. CL helicity of the mirrored heptamer nanostructure

We also measured the circularly polarized CL images of the mirrored heptamer structure. Figure S7a displays the SEM image of the structure. The LCP and RCP CL images are shown in Figure S7b, c, which were obtained by using the same setup as Figure S4a, b. It can be seen that the LCP (RCP) CL image for the mirrored structure has the mirrored pattern compared with the RCP (LCP) CL image in Figure S4a, b.

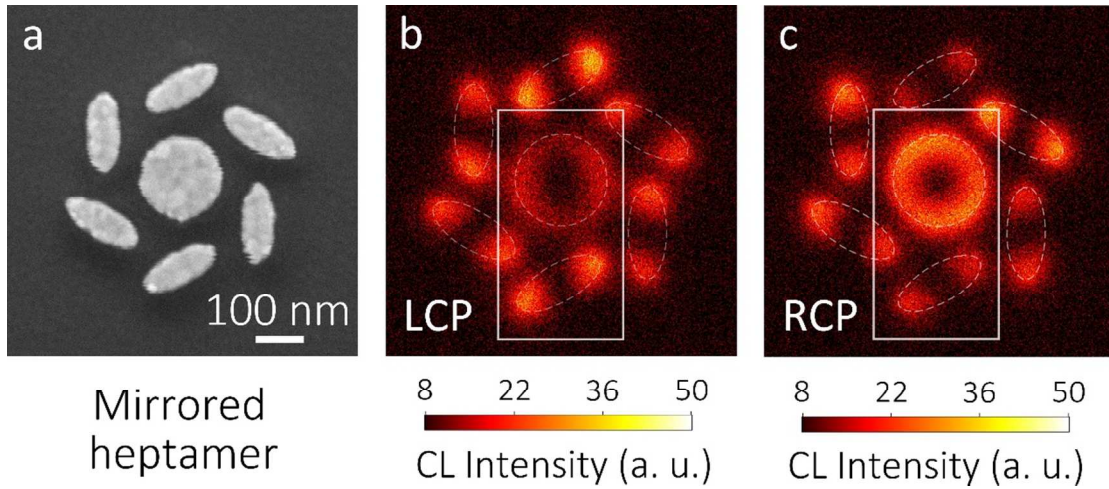


Figure S7. LCP and RCP CL images of the mirrored heptamer nanostructure. (a) SEM image of the mirrored heptamer. (b, c) LCP and RCP CL images of the mirrored heptamer acquired with the same optical path for Figure S4. Dashed lines depict the contour of the mirror heptamer.

VIII. CL chirality evolution with the heptamer changing from chiral to achiral

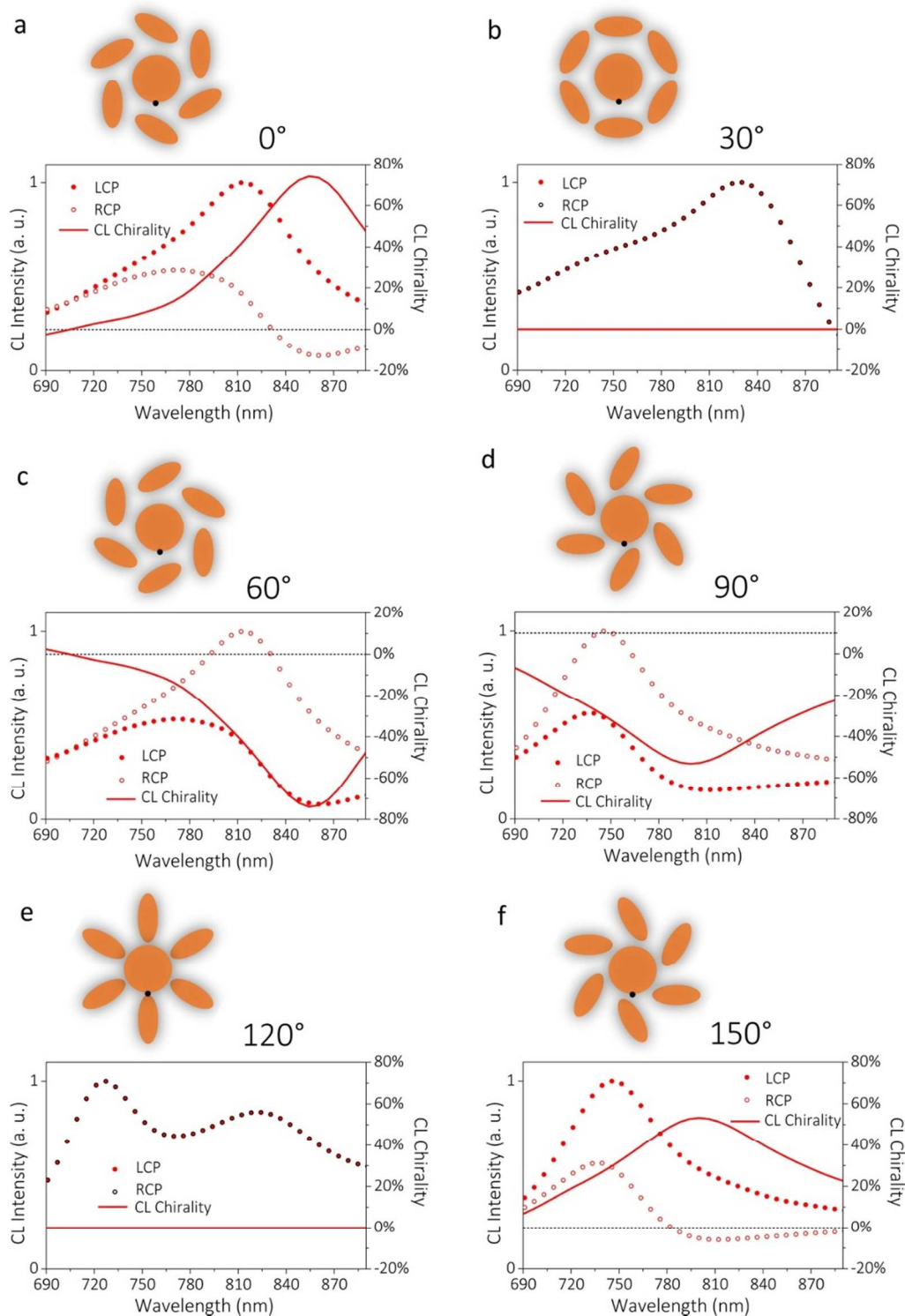


Figure S8. Simulated circularly polarized CL emissions of the heptamers with different ellipse rotation angle θ from 0° to 150° . The corresponding schematic of each heptamer are on the top

of the CL spectra with the impinging position fixed on the disk. With the largest structure symmetry breaking, the chirality reaches $\sim 75\%$ when θ is 0° and 60° with the sign of the CL chirality reversed. The CL chirality decreases to $\sim 50\%$ with the increasing of the structure symmetry, as θ is 120° and 150° , and finally disappears when θ changes to 30° and 120° .

REFERENCES

1. Fang, Y.; Verre, R.; Shao, L.; Nordlander, P.; Kall, M. *Nano letters* **2016**, 16, (8), 5183-5190.
2. Kaelberer, T.; Fedotov, V.; Papasimakis, N.; Tsai, D.; Zheludev, N. *Science* **2010**, 330, (6010), 1510-1512.
3. Radescu, E.; Vaman, G. *Physical Review E* **2002**, 65, (4), 046609.